Nanoscale

ROYAL SOCIETY OF CHEMISTRY

PAPER

View Article Online
View Journal | View Issue

Cite this: *Nanoscale*, 2023, **15**, 1347

AC-driven multicolor electroluminescence from a hybrid WSe_2 monolayer/AlGaInP quantum well light-emitting device†

Ya-Hui Chang,[a,b] Yen-Shou Lin,[a,b] Konthoujam James Singh,[b] Hsiang-Ting Lin,[a] Chiao-Yun Chang,[a,c] Zheng-Zhe Chen,[a,d] Yu-Wei Zhang,[a,e] Shih-Yen Lin,[a,e] Hao-Chung Kuo[a,b] and Min-Hsiung Shih *[a,b,f]

Light-emitting diodes (LEDs) are used widely, but when operated at a low-voltage direct current (DC), they consume unnecessary power because a converter must be used to convert it to an alternating current (AC). DC flow across devices also causes charge accumulation at a high current density, leading to lowered LED reliability. In contrast, gallium-nitride-based LEDs can be operated without an AC–DC converter being required, potentially leading to greater energy efficiency and reliability. In this study, we developed a multicolor AC-driven light-emitting device by integrating a WSe_2 monolayer and AlGaInP–GaInP multiple quantum well (MQW) structures. The CVD-grown WSe_2 monolayer was placed on the top of an AlGaInP-based light-emitting diode (LED) wafer to create a two-dimensional/three-dimensional heterostructure. The interfaces of these hybrid devices are characterized and verified through transmission electron microscopy and energy-dispersive X-ray spectroscopy techniques. More than 20% energy conversion from the AlGaInP MQWs to the WSe_2 monolayer was observed to boost the WSe_2 monolayer emissions. The voltage dependence of the electroluminescence intensity was characterized. Electroluminescence intensity–voltage characteristic curves indicated that thermionic emission was the mechanism underlying carrier injection across the potential barrier at the Ag–WSe_2 monolayer interface at low voltage, whereas Fowler–Nordheim emission was the mechanism at voltages higher than approximately 8.0 V. These multi-color hybrid light-emitting devices both expand the wavelength range of 2-D TMDC-based light emitters and support their implementation in applications such as chip-scale optoelectronic integrated systems, broad-band LEDs, and quantum display systems.

Received 7th July 2022,
Accepted 21st November 2022

DOI: 10.1039/d2nr03725d

rsc.li/nanoscale

Introduction

Transition metal dichalcogenides (TMDCs) are a class of two-dimensional (2D) materials composed of a transition-metal-atom layer sandwiched between two chalcogen-atom layers. Compared with the zero-bandgap material, graphene, 2D TMDCs have a direct bandgap with only one monolayer of metal atoms.[1–4] This endows them with greater potential for light-emitting applications due to their unique optoelectronic properties, such as layer-dependent bandgaps and large exciton binding energy. In light emission applications, high quantum efficiency is crucial and is achieved using a direct bandgap material as the emitter. Additionally, the atomic-scale thickness of TMDCs makes them suitable for many chip-scale optoelectronic applications.[5,6] The lack of surface dangling bonds in their atomic layers allows TMDCs to be integrated with a three-dimensional (3D) bulk material to create 2D/3D heterojunction devices without lattice matching being required.[6–9] Many works have indicated the potential of TMDCs for light-emitting modulators due to their short exciton lifetime.[10–16]

TMDC-based light-emitting devices with various structures have been demonstrated by several groups.[17–21] The structures of electroluminescent (EL) devices based on 2D TMDC materials can be mainly divided into two types in accordance with the driving source: (i) p–n junction structures and (ii)

[a]*Research Center for Applied Sciences (RCAS), Academia Sinica, Taipei 11529, Taiwan. E-mail: mhshih@gate.sinica.edu.tw*
[b]*Department of Photonics and Institute of Electro-Optical Engineering, College of Electrical and Computer Engineering, National Yang Ming Chiao Tung University, Hsinchu 30010, Taiwan*
[c]*Department of Electrical Engineering, National Taiwan Ocean University, Keelung 202301, Taiwan*
[d]*Department of Physics, National Taiwan University, Taipei, Taiwan, Taipei 10617, Taiwan*
[e]*Graduate Institute of Electronics Engineering, National Taiwan University, Taipei 10617, Taiwan*
[f]*Department of Photonics, National Sun Yat-sen University, Kaohsiung 80424, Taiwan*

† Electronic supplementary information (ESI) available. See DOI: https://doi.org/10.1039/d2nr03725d

capacitor structures.[22] The p–n junction structures, formed through lateral stacking of p- and n-type semiconductors, are generally operated from a direct current (DC) voltage source. In such structures, electrons and holes are injected simultaneously into a TMDC from two electrode terminals when a bias voltage is applied.[23–29]

TMDC materials with a p–n junction structure are typically produced using mechanical exfoliation, limiting their applications in large-scale devices and systems. The complex heterostructure and small size of exfoliated TMDC flakes make the p–n junction structures unsuitable for highly efficient industrial-scale production.[30] Moreover, one of the major bottlenecks experienced in the field of 2D TMDC-based electronics is the ultrahigh metal–TMDC contact resistance (of the order of several kilo-ohms to megaohms), which is due to the formation of a Schottky barrier at the metal–TMDC interface. The large metal–TMDC contact resistance causes inefficiency in carrier injection.[31,32] Many studies have reported that this contact resistance can be lowered through various strategies, such as the selection of an appropriate contact metal, doping, insertion of a space layer at the interface, and leveraging the contact geometry.[33–37] However, these methods increase the complexity of manufacturing processes.

Under alternating current (AC) pulsed voltage operating conditions, TMDC-based EL devices are typically fabricated with capacitor structures and consist of an insulating layer placed between the emission layer and the substrate. AC-driven EL devices have advantages over DC-driven devices; for instance, the vertically stacked capacitor structure is simpler than the p–n junction structure, and TMDC monolayers can be synthesized on a substrate directly through chemical vapor deposition (CVD), which is suitable for high-efficiency, low-cost, and large-scale light-emitting applications.[20,27,38,39] Most crucially, the carrier injection performance at the metal–TMDC interface when AC pulsed voltage is applied is almost independent of the Schottky barrier's height. Thus, efficient carrier injection can be achieved.[40]

The capacitor structure originated from strong-field EL devices, and were first developed in 1936 by George Destriau, who demonstrated the light emission of ZnS powder when a large electric field was applied.[41] Many studies have detailed construction of AC-driven EL devices with versatile emitting materials, ranging from inorganic thick semiconductors to organic atom-thin semiconductors, and such devices are considered promising alternatives to DC-driven EL devices.[42–50]

In addition to some scholars investigating AC-driven EL devices based on 2D-TMDCs, other groups have fabricated traditional III-nitride semiconductor-based light-emitting diodes (LEDs) driven by an AC voltage. LEDs have existed since 1962 and have been used in numerous fields, such as displays for electronics, lighting, and optical communication. However, LEDs and most electronic devices are operated with low-voltage DC, which is obtained using an AC–DC converter to convert 110/220 V AC voltage. This process of conversion causes unnecessary power consumption at magnitudes of 15%–30%. Moreover, a DC flow across devices causes charge accumulation at high current density, and such an accumulation influences the reliability of LEDs. Some of the latest research has demonstrated that gallium nitride (GaN)-based LEDs can be operated without an AC–DC converter being required, revealing their potential for application in energy-efficient and reliable LED lighting systems.[51–56] Although AC-driven TMDC monolayer LEDs have been demonstrated recently, it is worth noting that several important issues, such as device upscaling difficulty and a small emission area, still remain unresolved at the current stage.

In this paper, we present a two-color AC-driven light-emitting device with a capacitor structure composed of a CVD-grown WSe_2 monolayer on top of an AlGaInP-based LED wafer to form a 2D/3D heterostructure. An AlO_x insulating layer is inserted between these two materials to prevent carrier leakage.

Results and discussion

An optical microscopy image of the WSe_2 film grown on a sapphire substrate is presented in Fig. 1(a). Prior to the film's transfer, the number of layers in the CVD-grown WSe_2 flakes was characterized through atomic force microscopy (AFM) and Raman spectroscopy. The inset in Fig. 1(b) shows an AFM topography image of a WSe_2 flake; the image was acquired in tapping mode and in ambient air. The curve presented in Fig. 1(b) tracks the height profile along the yellow line. This height profile shows that the average step height between the sapphire substrate and the WSe_2 flakes was approximately 0.68 nm. This thickness value is in favorable agreement with previously reported values for a WSe_2 monolayer.

To verify the optical properties of WSe_2 on sapphire, a Raman spectrum was obtained with a 488 nm continuous-wave laser (Fig. 1(c)). The Raman spectrum shows two distinct peaks at 250.3 and 260 cm^{-1}, respectively, which are labelled E^1_{2g} and A_{1g}. The E^1_{2g} peak was generated by the in-plane vibration of tungsten and sulfur atoms, whereas the A_{1g} peak corresponded to the out-of-plane vibration of selenium atoms. The observed peaks in the Raman spectrum are consistent with previous reports. A B^1_{2g} peak at approximately 310 cm^{-1}, which represents an interlayer interaction between the different WSe_2 atomic layers, was not observed. This is indicative of WSe_2 monolayers grown on a sapphire substrate. The AFM images and Raman spectrum were used to determine the number of WSe_2 layers. The WSe_2 monolayer grown on sapphire was then transferred onto an AlGaInP quantum well LED epilayer covered by an AlO_x layer of thickness 30 nm. The optical microscope image of the transferred CVD-grown WSe_2 monolayer, with the transfer being achieved using the PMMA-assisted transfer method, is displayed in Fig. 1(d). Fig. 1(e) shows the PL spectrum of the hybrid WSe_2 monolayer/GaP-based structure by using a 532 nm wavelength laser. Two strong emission peaks associated with the AlGaInP quantum wells and the WSe_2 monolayer are observed. To verify the emission properties of the WSe_2 monolayer before and after the transfer process, the PL spectra of the transferred and as-grown WSe_2 monolayers are

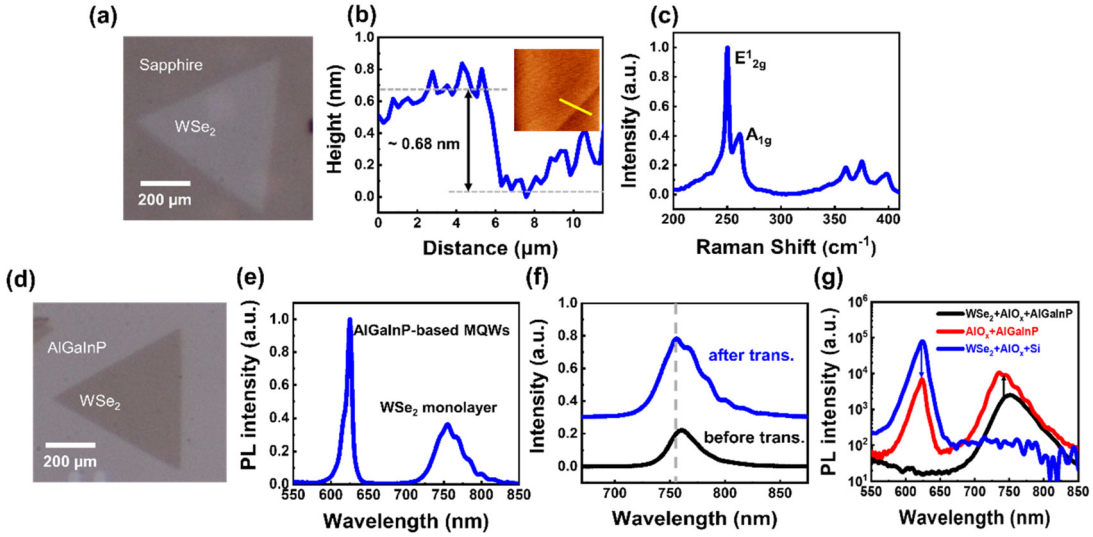

Fig. 1 (a) Optical microscopy image of an as-grown WSe_2 flake on sapphire. (b) AFM height profile of WSe_2–AlGaInP (inset: AFM image of the sample). (c) Raman spectrum of the as-grown WSe_2 flake on sapphire. (d) Optical microscopy image of the transferred WSe_2 flake. (e) PL spectrum of monolayered WSe_2–AlGaInP-based multiple quantum wells (MQWs). (f) PL spectra of the as-grown WSe_2 and transferred WSe_2. (g) PL spectra of the AlGaInP QWs (the blue line), WSe_2 (the black line), and hybrid AlGaInP QW/WSe_2 monolayer (the red line).

characterized, and shown in Fig. 1(f). Compared with the spectrum of the as-grown WSe_2 monolayer sample, that of the transferred WSe_2 monolayer shows a peak that is blue-shifted. This small blue shift is attributed to the release of strain during the transfer process, where strain was caused by the difference in the thermal expansion coefficients of the CVD-grown WSe_2 monolayer and sapphire substrate. The small oscillations in the PL spectrum are due to Fabry–Perot oscillations from the bottom AlGaInP MQW structure.

To investigate the interactions between the WSe_2 monolayer and the AlGaInP QWs, we transferred WSe_2 monolayers to the AlGaInP QW substrate and the AlO_x substrate and characterized the PL spectra of the two WSe_2 devices and the AlGaInP QW device. Fig. 1(g) shows the PL spectra of the AlGaInP QW (the blue solid line), the WSe_2 monolayer (the black solid line) on AlO_x substrate, and the hybrid WSe_2 monolayer/AlGaInP QW (the red line) devices. The color conversion phenomena associated with the AlGaInP QWs and the WSe_2 monolayer were observed. If the QWs and WSe_2 monolayer were integrated into a single device, the corresponding PL intensities were reduced in the AlGaInP QW emission region but enhanced in the WSe_2 emission region compared with the individual gain spectra. This result can be attributed to the energy transfer from the high energy medium (*i.e.* the AlGaInP QWs in the study) to the low energy medium (the WSe_2 monolayer in the study).[57,58] The color conversion efficiency η can be calculated as follows:

$$\eta = \frac{\int_{700}^{850} I_{\mathrm{QWs+WSe_2}}\mathrm{d}\lambda - \int_{700}^{850} I_{\mathrm{WSe_2}}\mathrm{d}\lambda}{\int_{550}^{700} I_{\mathrm{QWs}}\mathrm{d}\lambda - \int_{550}^{700} I_{\mathrm{QWs+WSe_2}}\mathrm{d}\lambda} \times 100\%, \quad (1)$$

where I_{QWs}, $I_{\mathrm{WSe_2}}$, and $I_{\mathrm{QWs+WSe_2}}$ are, respectively, the PL intensity magnitudes of AlGaInP QWs, WSe_2, and the hybrid QW/WSe_2 monolayer at various wavelengths λ. For the hybrid LED device, the corresponding energy conversion efficiency η is approximately 20.98%.

Electrical measurements were conducted at room temperature and under ambient conditions by using arbitrary function generators to generate AC pulse square waves for driving the devices. The devices were connected to two probe stations, which contained tungsten probe tips for electrical testing. The signal was observed using a microscope objective lens. The signal passed through the 20 μm-wide entrance slit of the spectrometer and was then focused on a 600 g mm^{-1} grating to separate the light signal into spatial spectra.

A 3D schematic and the vertical structure of the WSe_2 monolayer–AlGaInP-based light-emitting device are shown in Fig. 2(a) and (b), respectively. The device consists of four components: two silver electrodes, emitter layers, and an insulating layer. The emitter layers comprise a WSe_2 monolayer and the AlGaInP–GaInP multiple quantum well (MQW) active region. One of the electrodes serves as the bottom gate, while the other electrode serves as the source contact. Carriers are injected at the interface between the source contact and the semiconductor. To introduce an electric field into the insulating layer, a high-dielectric-constant AlO_x film is selected as the insulating layer. The WSe_2 monolayer is transferred onto the AlGaInP-based LED epilayer with an AlO_x film inserted between the WSe_2 monolayer and the LED epilayer to serve as a capacitive component. Electrodes are deposited on the top of the WSe_2 layer and the surface of the bare LED epilayer to act as the source and gate electrodes, respectively. The left side of Fig. 2(c) shows the top-view scanning electron microscopy (SEM) image of the device at a magnification of 7000×. The geometry of the top electrode is a simple square window. The

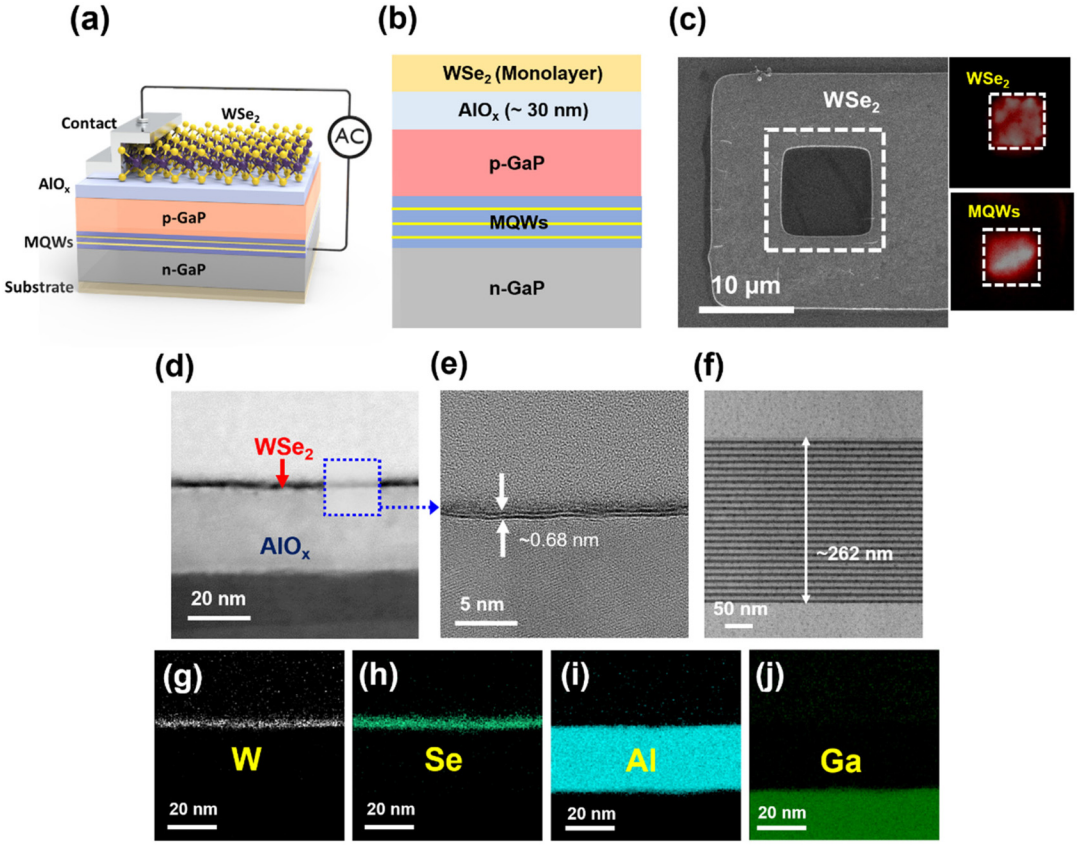

Fig. 2 (a) Schematic of the hybrid WSe_2 monolayer/AlGaInP-QW based light-emitting device. (b) Cross-sectional view of the device's structure. (c) SEM top view of the fabricated device (the dashed white line marks the region of transferred WSe_2) and the intensity distributions of light emission from the device captured using a CCD camera. No color information is given in the images. (d) Cross-sectional BF-STEM image of the fabricated device. (e) Higher magnification of the square area within the dotted blue line in (d). (f) Cross-sectional TEM image of the AlGaInP–GaInP MQWs. The EDX mapping images and elemental analysis for (g)W, (h) Se, (i) Al and (j) Ga.

dark area enclosed by the dashed white line is the transferred WSe_2 monolayer. Images of light emission from the device, captured using a charge-coupled device (CCD) camera, are shown on the right side of Fig. 2(c). The spatial distribution of the intensity of light emitted by the WSe_2 monolayer and AlGaInP-based MQWs was nonuniform, which resulted from current crowding effects. In the WSe_2 monolayer, this was because carrier injection and recombination occurred near the edge of the electrode. The thickness and composition of the layers in the device were determined through transmission electron microscopy (TEM) and energy-dispersive X-ray spectroscopy (EDX). Checking the thickness of WSe_2 was extremely important because its properties strongly depend on the number of layers. Fig. 2(d) shows a bright-field scanning transmission electron microscopy (BF-STEM) image of the WSe_2–AlO_x–AlGaInP layered structure. Fig. 2(e) and (f) show the higher-magnification TEM images of the square area within the dotted blue line in Fig. 2(d) and of the GaInP–AlGaInP MQWs, respectively. The cross-sectional TEM image of WSe_2 reveals that the thickness of single-layered WSe_2 was approximately 0.7 nm, which perfectly matches the previous report of a monolayered WSe_2 thickness. To further characterize the elemental composition of the layered structure, EDX was performed. The EDX elemental mapping images of WSe_2–AlO_x–AlGaInP shown in Fig. 2(g)–(j) indicate the spatial distribution of various elements over the structure. The distributions of W and Se were uniform. In addition, the presence of Al and Ga was expected due to the presence of the AlO_x insulating layer and substrate of the AlGaInP-based LED.

Fig. 3(a) shows the room-temperature EL spectra of the WSe_2–AlGaInP-based light-emitting device driven by various voltages at a fixed frequency. For both the AlGaInP-based LED and WSe_2, the EL intensity increased with the voltage. The inset of Fig. 3(a) shows the EL spectra for WSe_2 emission at 1 MHz with increasing voltage. The spectra contain two distinguishable emission peaks at approximately 627 and 755 nm, corresponding to the AlGaInP-based MQWs and WSe_2 monolayer, respectively. Because of the poor emission efficiency of the WSe_2 monolayer, the EL peak intensity of WSe_2 has been multiplied by a factor of 10 to better enable visualization. The peak at a wavelength of 627 nm in the red emission band with a full width at half maximum linewidth of 10 nm was attributed to the AlGaInP–InGaP MQWs, whereas the peak at a longer wavelength was attributed to the direct

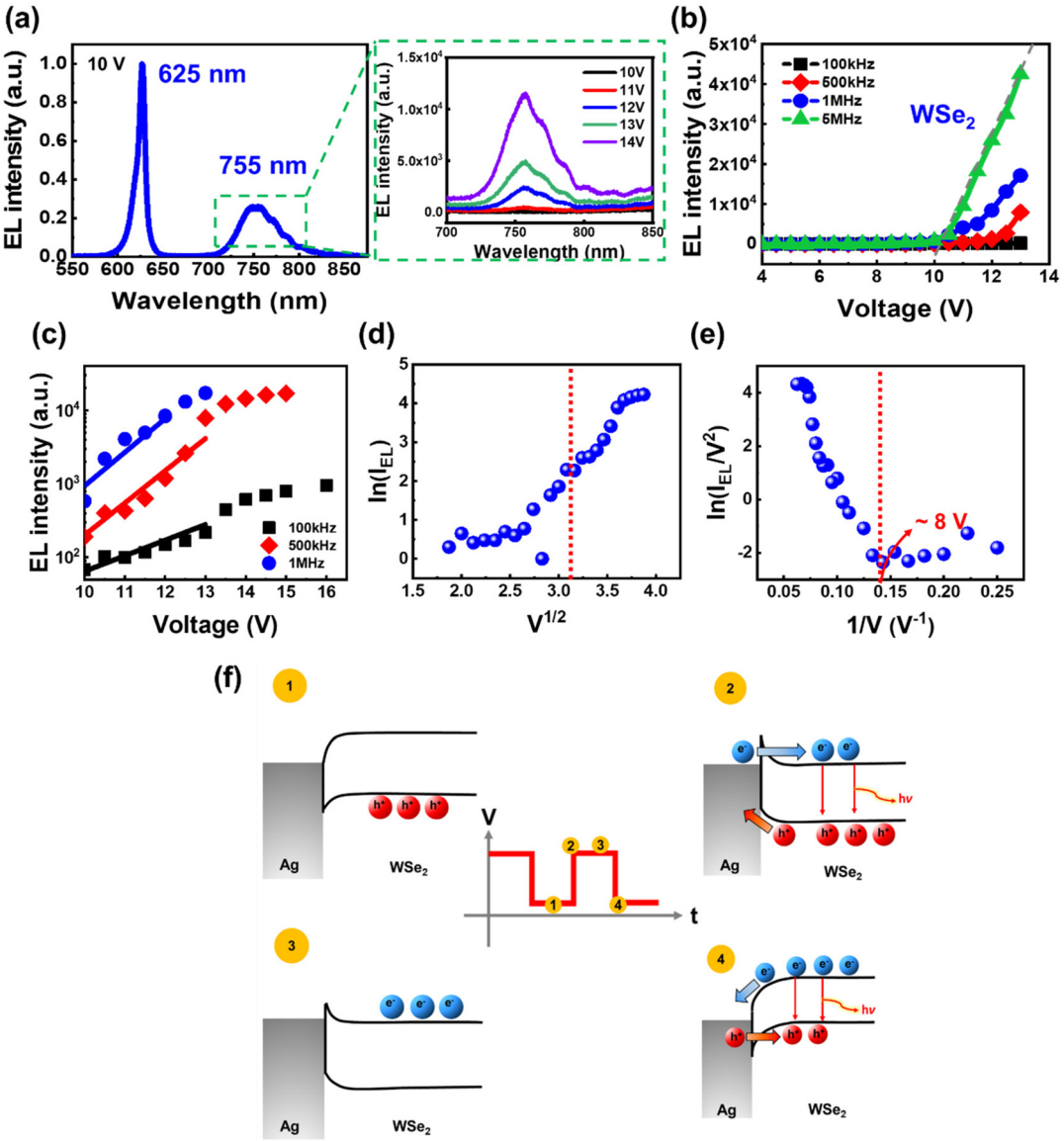

Fig. 3 (a) EL spectra of the device at various voltages at a fixed frequency (WSe_2 emission at 1 MHz). (b) Voltage-dependent EL intensity of WSe_2. (c) Semi-log plot of the voltage-dependent EL intensity of WSe_2. EL intensity–voltage characteristic curves showing (d) Schottky emission and (e) FN emission at the metal–WSe_2 interface. (f) Schematic band diagram of the metal–WSe_2 interface upon a change in polarity of the AC voltage.

intralayer exciton emission of monolayered WSe_2, in good agreement with previous works.[59,60] The small oscillation due to Fabry–Perot interferences in the QW layer was also observed in the EL spectrum.

Fig. 3(b) shows the voltage-dependent peak EL intensity of WSe_2 at constant frequencies. The EL intensity increases clearly as the operating voltage becomes larger than the threshold voltage. The threshold voltage (V_{th}) of the WSe_2 monolayer, defined as the x-intercept of the linear portion of the EL intensity–voltage curve, was approximately 10 V (green line in Fig. 3(b)). As the operating frequency increases, the threshold voltage of the WSe_2 monolayer emission decreases. No light emission was observed at voltages below V_{th} due to insufficient carrier injection from the Ag electrode. The EL intensity of WSe_2 was proportional to the voltage above V_{th}. Recent studies have proposed the following empirical model of the relationship between the EL intensity and the voltage: $I_{EL} \propto \exp(\alpha\kappa V)$,[61] where κ is the constant of the injected carrier concentration in the 2D semiconductor and α is the constant related to the characteristics of excitons. A semi-log plot of the EL intensity as a function of voltage is displayed in Fig. 3(c). This figure indicates a linear relationship between the logarithm of the EL intensity and the voltage, which conforms to the aforementioned model.

Research has revealed that thermionic emission and Fowler–Nordheim (FN) emission are the main mechanisms underlying charge transport through the Schottky contact at a metal–2D-material interface.[62,63] The carrier injection

efficiency is severely limited by the Schottky barrier at the metal–TMDC interface. To examine the mechanism of charge injection through the interface between the electrode and WSe_2 under external electric field and room temperature conditions, we plotted $\ln(I_{EL})$ *versus* $V^{1/2}$ and $\ln(I_{EL}/V^2)$ *versus* V^{-1}. These curves represent thermionic-emission-like and FN-like behaviors, respectively. Thermionic emission is usually considered to occur at high temperatures; charges can acquire sufficient energy to overcome the Schottky barrier. When thermionic emission occurs without the presence of an external electric field, the current density can be described as a function of temperature, as in the Richardson–Dushman equation.[64] However, if the effect of an electric field is considered, the current density can be expressed by a Schottky equation:[65]

$$I(T,V) = AT^2 \exp\left(-\frac{\phi - (ke^3v)^{\frac{1}{2}}}{k_B T}\right) \quad (2)$$

where A is the Richardson coefficient, T is the temperature, ϕ is the work function, k_B is Boltzmann's constant, and V is the amplitude of the voltage. At constant temperature and in a weak electric field, this equation can be simplified to $I(V) = I_{SE}\exp(A\sqrt{V})$.

According to the Schottky equation, the logarithmic EL intensity is proportional to the square root of the voltage. The thermionic emission plot, displayed in Fig. 3d, shows that the relationship between $\ln(I_{EL})$ and $V^{1/2}$ is positive and linear in the low-voltage range ($V < V_{th}$; left-hand side of the red dotted line). Therefore, thermionic emission was considered to be the mechanism underlying carrier injection across the potential barrier at the Ag–WSe_2 interface at a low voltage.

When a strong field is considered, carriers can tunnel through the barrier by a quantum mechanical effect. In quantum mechanical theory, the possibility of an electron penetrating a potential barrier is described by:[66,67]

$$T(E) = \exp\left[-\frac{4}{3}\frac{\sqrt{2m}\Phi^{3/2}}{\hbar eE}\right] \quad (3)$$

where m is the effective mass, Φ is the barrier height, $\hbar$ is Planck's constant divided by 2π, and E is the electric field strength. The tunneling current is proportional to the electron tunneling probability. By fitting the experimental data with the equation in the low field region, the Schottky barrier height is approximately 42.3 meV. The estimated value is consistent with the reported values.[8,20,68–70]

The tunneling probability depends on the width of the barrier. According to the barrier width equation $x = \Phi/eE$, the width of barrier x is narrow when a strong electric field is applied. The tunneling of carriers occurs when the magnitude of the electric field is sufficiently high to change the barrier from being a flat band to having a triangular shape with a narrow effective width. This type of tunneling mechanism is known as FN tunneling.

The FN tunneling current equation is:

$$J = \alpha E^2 \exp\left(\frac{-\beta}{E}\right) \quad (4)$$

where J is the electric-field-induced tunneling current, E is the external electric field strength, and α and β are constants. Fig. 3(e) shows a plot of $\ln(I_{EL}/V^2)$ *versus* V^{-1}. In this plot, the EL intensity and reciprocal of the voltage ($1/V$) are negatively and linearly related at voltages above approximately 8 V. The negative linear region of the FN plot is limited in a given range. When the electric field is weak, the electrons do not acquire sufficiently large energy to overcome the potential barrier; thus, the magnitude of the direct tunneling current is low.

The AC-voltage-driven electroluminescence mechanism of 2D materials has been investigated previously.[20,27,40] Fig. 3(f) shows a schematic explaining the mechanism of electroluminescence of WSe_2. In brief, by applying a steady negative bias to the back-gate electrode, holes accumulate at WSe_2 and the Schottky barrier blocks the flow of holes from WSe_2 to the metal electrode (Fig. 3(f), part marked 1). When the AC square-wave pulse signal changes from a negative to a positive polarity, the capacitive elements (*i.e.*, AlO_x) induce a potential difference between the top source and the back gate. The potential drop across the WSe_2 layer causes conduction band bending and then leads to the tunneling of electrons from the electrode to WSe_2. Subsequently, the holes generated in the previous step recombine with the injected electrons, which causes the release of a photon (Fig. 3(f), part marked 2). The same behavior is observed when the voltage switches from a positive to a negative polarity (Fig. 3(f), parts marked 3 and 4).

The peak values in the spectra presented in Fig. 3(a) were recorded, and the relationship between the EL intensity of the AlGaInP-based MQWs and the peak-to-peak voltage was discovered (Fig. 4(a) and (b)). By extrapolating the EL intensity–voltage curves, a threshold voltage of approximately 5.5 V was obtained. The EL intensity of the AlGaInP-based MQWs follows an empirical equation:

$$L = L_0 \exp(-\beta/V^{1/2}) \quad (5)$$

where L_0 and β are two material-dependent constants.

The empirical equation fitted the experimental data favorably and indicated that the EL intensity increased superlinearly with an increase in the voltage.[71,72] The EL peak intensity of both the AlGaInP-based LED and WSe_2 was strongly dependent on voltage rather than current due to the capacitance characteristics of the device.[73]

Ag–AlO_x–AlGaInP has a metal–insulator–semiconductor (MIS) structure. It comprises an insulating layer (AlO_x) that separates the metal electrode and semiconductor. The process of radiative recombination in an AlGaInP-based LED[53,74] is given as follows. When a positive AC bias voltage is applied to the gate electrode, the majority of carriers (holes) from the p-type region of the AlGaInP LED accumulate at the AlO_x–p-GaP interface. The accumulated carriers cannot be injected into the Ag metal from the semiconductor because of the tunnel barrier, which is an insulating layer of AlO_x with a thickness of a few tens of nanometers. The electrons can

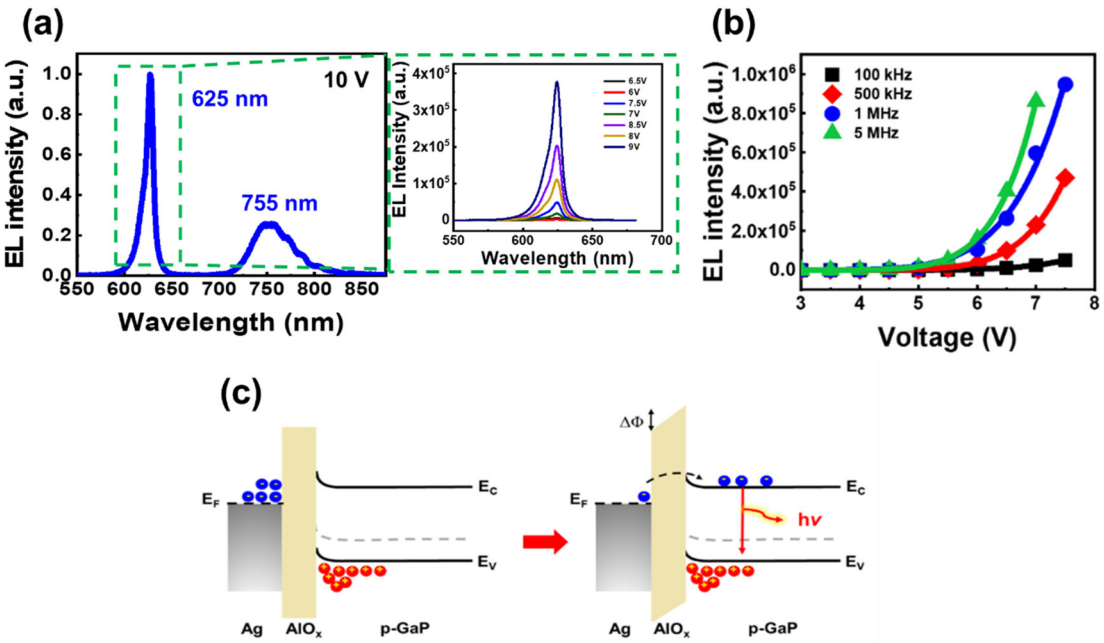

Fig. 4 (a) EL spectra of the device at various voltages at a fixed frequency (AlGaInP-based MQW emission at 1 MHz). (b) Voltage-dependent EL intensity of AlGaInP-based MQWs. (c) Energy band diagram of the MIS structure of Ag–AlO_x–p-GaP under zero bias and high bias conditions.

tunnel from the electrode to the semiconductor when a high positive voltage is applied because this reduces the effective barrier width (FN tunneling). Finally, the electrons recombine with holes and release energy in the form of a photon (as illustrated in Fig. 4(c)).

By estimating the internal quantum efficiency and the extraction efficiency of the devices, the external quantum efficiency (EQE) of the WSe_2 monolayer and AlGaInP QWs devices are approximately 0.018% and 0.056%, as given in Fig. S2 and S3 of the ESI.† The device is operated under ambient conditions and no significant drop in efficiency was observed. It is worth noting that because the external quantum efficiency of the AlGaInP QW LED is larger than that of a WSe_2 monolayer, the thickness of the AlO_x layer, deposited through atomic layer deposition, can be controlled to manipulate the ratio of the EL intensity of the AlGaInP QWs to that of the WSe_2 monolayer by controlling the light extraction efficiency and the threshold voltage. This is an important step to counterbalance the EL intensities of the AlGaInP QWs and the WSe_2 monolayer. However, two-color emission was still achieved at a voltage greater than 10 V in the study. The AC driving conditions, and the device structure, can be further optimized in the future for better multi-color emission from the hybrid LED device.

Conclusions

In summary, we developed a multicolor AC-driven light-emitting device by integrating a WSe_2 monolayer and AlGaInP–GaInP multiple quantum well (MQW) structures. The CVD-grown WSe_2 monolayer was placed on the top of an AlGaInP-based light-emitting diode (LED) wafer to create a two-dimensional/three-dimensional heterostructure. The insulating layer, comprising AlO_x, which was deposited through atomic layer deposition, is placed between these two materials and serves as a capacitor. The interfaces of the hybrid devices are characterized and verified with TEM images and EDX techniques. The device's room-temperature electroluminescence spectrum was found to contain two peaks that correspond to the emissions by the WSe_2 monolayer and AlGaInP–InGaP MQWs, respectively. The voltage dependence of the electroluminescence intensity was characterized. The electroluminescence intensity–voltage characteristic curves indicated that thermionic emission was the mechanism underlying carrier injection across the potential barrier at the Ag–WSe_2 monolayer interface at a low voltage, whereas Fowler–Nordheim emission was the mechanism at voltages higher than approximately 8.0 V. These multi-color hybrid light-emitting devices both expand the wavelength range of 2-D TMDC-based light emitters and support their implementation in applications such as chip-scale optoelectronic integrated systems, broad-band LEDs, and quantum display systems.

Conflicts of interest

The authors declare no competing financial interest.

Acknowledgements

This work was supported by research funding from Academia Sinica in Taiwan and the Ministry of Science and Technology

(MOST) in Taiwan under Contract numbers MOST 110-2112-M-001-053 and MOST 111-2112-M-001-078.

References

1 A. Kuc, N. Zibouche and T. Heine, Influence of quantum confinement on the electronic structure of the transition metal sulfideTS2, *Phys. Rev. B: Condens. Matter Mater. Phys.*, 2011, **83**, 245213.
2 K. F. Mak, C. Lee, J. Hone, J. Shan and T. F. Heinz, Atomically thin MoS(2): a new direct-gap semiconductor, *Phys. Rev. Lett.*, 2010, **105**(13), 136805.
3 A. Splendiani, L. Sun, Y. Zhang, T. Li, J. Kim, C. Y. Chim, G. Galli and F. Wang, Emerging photoluminescence in monolayer MoS2, *Nano Lett.*, 2010, **10**(4), 1271–1275.
4 P. Tonndorf, R. Schmidt, P. Bottger, X. Zhang, J. Borner, A. Liebig, M. Albrecht, C. Kloc, O. Gordan, D. R. Zahn, S. Michaelis de Vasconcellos and R. Bratschitsch, Photoluminescence emission and Raman response of monolayer MoS(2), MoSe(2), and WSe(2), *Opt. Express*, 2013, **21**(4), 4908–4916.
5 D. Andrzejewski, R. Oliver, Y. Beckmann, A. Grundmann, M. Heuken, H. Kalisch, A. Vescan, T. Kümmell and G. Bacher, Flexible Large–Area Light–Emitting Devices Based on WS2Monolayers, *Adv. Opt. Mater.*, 2020, **8**, 2000694.
6 F. Withers, O. Del Pozo-Zamudio, A. Mishchenko, A. P. Rooney, A. Gholinia, K. Watanabe, T. Taniguchi, S. J. Haigh, A. K. Geim, A. I. Tartakovskii and K. S. Novoselov, Light-emitting diodes by band-structure engineering in van der Waals heterostructures, *Nat. Mater.*, 2015, **14**(3), 301–306.
7 S. H. Bae, H. Kum, W. Kong, Y. Kim, C. Choi, B. Lee, P. Lin, Y. Park and J. Kim, Integration of bulk materials with two-dimensional materials for physical coupling and applications, *Nat. Mater.*, 2019, **18**(6), 550–560.
8 Y. Liu, N. O. Weiss, X. Duan, H.-C. Cheng, Y. Huang and X. Duan, van der Waals heterostructures and devices, *Nat. Rev. Mater.*, 2016, **1**, 16042.
9 W. Zhang, Q. Wang, Y. Chen, Z. Wang and A. T. S. Wee, van der Waals stacked 2D layered materials for optoelectronics, *2D Mater.*, 2016, **3**, 022001.
10 R. Cheng, S. Jiang, Y. Chen, Y. Liu, N. Weiss, H.-C. Cheng, H. Wu, Y. Huang and X. Duan, Few-layer molybdenum disulfide transistors and circuits for high-speed flexible electronics, *Nat. Commun.*, 2014, **5**(1), 5143.
11 X. Geng, Y. Yu, X. Zhou, C. Wang, K. Xu, Y. Zhang, C. Wu, L. Wang, Y. Jiang and Q. Yang, Design and construction of ultrathin MoSe2 nanosheet-based heterojunction for high-speed and low-noise photodetection, *Nano Res.*, 2016, **9**(9), 2641–2651.
12 D. Kwak, M. Paur, K. Watanabe, T. Taniguchi and T. Mueller, High-Speed Electroluminescence Modulation in Monolayer WS2, *Adv. Mater. Technol.*, 2022, **7**(5), 2100915.
13 C. T. Phare, Y.-H. Daniel Lee, J. Cardenas and M. Lipson, Graphene electro-optic modulator with 30 GHz bandwidth, *Nat. Photonics*, 2015, **9**(8), 511–514.
14 F. Sun, C. Nie, X. Wei, H. Mao, Y. Zhang and G. P. Wang, All-optical modulation based on MoS2-Plasmonic nanoslit hybrid structures, *Nanophotonics*, 2021, **10**(16), 3957–3965.
15 Z. Sun, A. Martinez and F. Wang, Optical modulators with 2D layered materials, *Nat. Photonics*, 2016, **10**(4), 227–238.
16 Y. Wang, F. Zhang, X. Tang, X. Chen, Y. Chen, W. Huang, Z. Liang, L. Wu, Y. Ge, Y. Song, J. Liu, D. Zhang, J. Li and H. Zhang, All-Optical Phosphorene Phase Modulator with Enhanced Stability Under Ambient Conditions, *Laser Photonics Rev.*, 2018, **12**(6), 1800016.
17 O. Lopez-Sanchez, E. Alarcon Lladó, V. B. Koman, A. Fontcuberta i Morral, A. Radenovj and A. J. A. N. Kis, Light Generation and Harvesting in a van der Waals Heterostructure, *ACS Nano*, 2014, **8**, 3042–3048.
18 J. Gu, B. Chakraborty, M. Khatoniar and V. M. Menon, A room-temperature polariton light-emitting diode based on monolayer WS2, *Nat. Nanotechnol.*, 2019, **14**(11), 1024–1028.
19 Y. Li, H. Sun, L. Gan, J. Zhang, J. Feng, D. Zhang and C.-Z. Ning, Optical Properties and Light-Emission Device Applications of 2-D Layered Semiconductors, *Proc. IEEE*, 2020, **108**(5), 676–703.
20 D. H. Lien, M. Amani, S. B. Desai, G. H. Ahn, K. Han, J. H. He, J. W. Ager 3rd, M. C. Wu and A. Javey, Large-area and bright pulsed electroluminescence in monolayer semiconductors, *Nat. Commun.*, 2018, **9**(1), 1229.
21 Y. Zhu, X. Sun, Y. Tang, L. Fu and Y. Lu, Two-dimensional materials for light emitting applications: Achievement, challenge and future perspectives, *Nano Res.*, 2020, **14**(6), 1912–1936.
22 C. Wang, F. Yang and Y. Gao, The highly-efficient light-emitting diodes based on transition metal dichalcogenides: from architecture to performance, *Nanoscale Adv.*, 2020, **2**(10), 4323–4340.
23 J. S. Ross, P. Klement, A. M. Jones, N. J. Ghimire, J. Yan, D. G. Mandrus, T. Taniguchi, K. Watanabe, K. Kitamura, W. Yao, D. H. Cobden and X. Xu, Electrically tunable excitonic light-emitting diodes based on monolayer WSe2 p-n junctions, *Nat. Nanotechnol.*, 2014, **9**(4), 268–272.
24 J. S. Ross, P. Rivera, J. Schaibley, E. Lee-Wong, H. Yu, T. Taniguchi, K. Watanabe, J. Yan, D. Mandrus, D. Cobden, W. Yao and X. Xu, Interlayer Exciton Optoelectronics in a 2D Heterostructure p-n Junction, *Nano Lett.*, 2017, **17**(2), 638–643.
25 D. Andrzejewski, E. Hopmann, M. John, T. Kummell and G. Bacher, WS2 monolayer-based light-emitting devices in a vertical p-n architecture, *Nanoscale*, 2019, **11**(17), 8372–8379.
26 D. Andrzejewski, H. Myja, M. Heuken, A. Grundmann, H. Kalisch, A. Vescan, T. Kümmell and G. Bacher, Scalable Large-Area p–i–n Light-Emitting Diodes Based on WS2 Monolayers Grown via MOCVD, *ACS Photonics*, 2019, **6**(8), 1832–1839.
27 K. Han, G. H. Ahn, J. Cho, D.-H. Lien, M. Amani, S. B. Desai, G. Zhang, H. Kim, N. Gupta, A. Javey and M. C. Wu, Bright electroluminescence in ambient con-

ditions from WSe2 p-n diodes using pulsed injection, *Appl. Phys. Lett.*, 2019, **115**, 011103.
28 J. Wang, A. Rousseau, M. Yang, T. Low, S. Francoeur and S. Kena-Cohen, Mid-infrared Polarized Emission from Black Phosphorus Light-Emitting Diodes, *Nano Lett.*, 2020, **20**(5), 3651–3655.
29 H. Ou, H. Matsuoka, J. Tempia, T. Yamada, T. Takahashi, K. Oi, Y. Takaguchi, T. Endo, Y. Miyata, C. H. Chen, L. J. Li, J. Pu and T. Takenobu, Spatial Control of Dynamic p-i-n Junctions in Transition Metal Dichalcogenide Light-Emitting Devices, *ACS Nano*, 2021, **15**, 12911–12921.
30 A. J. Watson, W. Lu, M. H. D. Guimarães and M. Stöhr, Transfer of large-scale two-dimensional semiconductors: challenges and developments, *2D Mater.*, 2021, **8**, 032001.
31 G. Arutchelvan, C. J. Lockhart de la Rosa, P. Matagne, S. Sutar, I. Radu, C. Huyghebaert, S. De Gendt and M. Heyns, From the metal to the channel: a study of carrier injection through the metal/2D MoS2 interface, *Nanoscale*, 2017, **9**(30), 10869–10879.
32 D. Somvanshi, S. Kallatt, C. Venkatesh, S. Nair, G. Gupta, J. K. Anthony, D. Karmakar and K. Majumdar, Nature of carrier injection in metal/2D-semiconductor interface and its implications for the limits of contact resistance, *Phys. Rev. B*, 2017, **96**, 205423.
33 H. Choi, B. H. Moon, J. H. Kim, S. J. Yun, G. H. Han, S. G. Lee, H. Z. Gul and Y. H. Lee, Edge Contact for Carrier Injection and Transport in MoS2 Field-Effect Transistors, *ACS Nano*, 2019, **13**(11), 13169–13175.
34 A. Jain, A. Szabo, M. Parzefall, E. Bonvin, T. Taniguchi, K. Watanabe, P. Bharadwaj, M. Luisier and L. Novotny, One-Dimensional Edge Contacts to a Monolayer Semiconductor, *Nano Lett.*, 2019, **19**(10), 6914–6923.
35 N. Wang, Ohmic contacts for atomically-thin transition metal dichalcogenide semiconductors, *J. Semicond.*, 2020, **41**, 070401.
36 P. C. Shen, C. Su, Y. Lin, A. S. Chou, C. C. Cheng, J. H. Park, M. H. Chiu, A. Y. Lu, H. L. Tang, M. M. Tavakoli, G. Pitner, X. Ji, Z. Cai, N. Mao, J. Wang, V. Tung, J. Li, J. Bokor, A. Zettl, C. I. Wu, T. Palacios, L. J. Li and J. Kong, Ultralow contact resistance between semimetal and monolayer semiconductors, *Nature*, 2021, **593**(7858), 211–217.
37 Y. Zheng, J. Gao, C. Han and W. Chen, Ohmic Contact Engineering for Two-Dimensional Materials, *Cell Rep. Phys. Sci.*, 2021, **2**, 100298.
38 J. Cho, M. Amani, D. H. Lien, H. Kim, M. Yeh, V. Wang, C. Tan and A. Javey, Centimeter–Scale and Visible Wavelength Monolayer Light–Emitting Devices, *Adv. Funct. Mater.*, 2019, **30**, 1907941.
39 Y. Zhu, B. Wang, Z. Li, J. Zhang, Y. Tang, J. F. Torres, W. Lipinski, L. Fu and Y. Lu, A High-Efficiency Wavelength-Tunable Monolayer LED with Hybrid Continuous-Pulsed Injection, *Adv. Mater.*, 2021, **33**(29), e2101375.
40 V. Wang, Y. Zhao and A. Javey, Performance Limits of an Alternating Current Electroluminescent Device, *Adv. Mater.*, 2021, **33**(2), e2005635.
41 G. Destriau, AC electroluminescence in ZnS, *J. Chim. Phys.*, 1936, **33**, 578.
42 M. Bredol and H. Schulze Dieckhoff, Materials for Powder-Based AC-Electroluminescence, *Materials*, 2010, **3**(2), 1353–1374.
43 X. Cheng, Z. Zang, K. Yuan, T. Wang, K. Watanabe, T. Taniguchi, L. Dai and Y. Ye, A hybrid structure light-emitting device based on a $CsPbBr_3$ nanoplate and two-dimensional materials, *Appl. Phys. Lett.*, 2020, **116**, 263103.
44 P. B. W. Jensen, J. Kjelstrup-Hansen and H.-G. Rubahn, Multicolor nanofiber based organic light-emitting transistors, *Org. Electron.*, 2013, **14**(12), 3324–3330.
45 X. Liu, J. Kjelstrup-Hansen, H. Boudinov and H.-G. Rubahn, Charge-carrier injection assisted by space-charge field in AC-driven organic light-emitting transistors, *Org. Electron.*, 2011, **12**(10), 1724–1730.
46 X. Liu, I. Wallmann, H. Boudinov, J. Kjelstrup-Hansen, M. Schiek, A. Lützen and H.-G. Rubahn, AC-biased organic light-emitting field-effect transistors from naphthyl end-capped oligothiophenes, *Org. Electron.*, 2010, **11**(6), 1096–1102.
47 H. Kajii, M. Yoshinaga, T. Karaki, M. Morifuji and M. Kondow, Microcavity polymer electroluminescent devices with solution-processed dielectric distributed Bragg reflectors utilizing inorganic copper(I) thiocyanate and insulating polymers, *Org. Electron.*, 2021, **88**, 106011.
48 M. Fröbel, T. Schwab, M. Kliem, S. Hofmann, K. Leo and M. C. Gather, Get it white: color-tunable AC/DC OLEDs, *Light: Sci. Appl.*, 2015, **4**(2), e247–e247.
49 V. Wang and A. Javey, A Resonantly Driven, Electroluminescent Metal Oxide Semiconductor Capacitor with High Power Efficiency, *ACS Nano*, 2021, **15**(9), 15210–15217.
50 Y. Zhao, V. Wang, D.-H. Lien and A. Javey, A generic electroluminescent device for emission from infrared to ultraviolet wavelengths, *Nat. Electron.*, 2020, **3**(10), 612–621.
51 S. M. Sadaf, Y. H. Ra, H. P. Nguyen, M. Djavid and Z. Mi, Alternating-Current InGaN/GaN Tunnel Junction Nanowire White-Light Emitting Diodes, *Nano Lett.*, 2015, **15**(10), 6696–6701.
52 S. Zhou, Y. Gao, C. Zheng, Y. Liu, H. Hu, J. Lv and X. Liu, A Comparative Study of GaN-Based Direct Current and Alternating Current High Voltage Light-Emitting Diodes, *Phys. Status Solidi A*, 2018, **215**, 1700554.
53 M. Hartensveld, B. Melanson, V. Thirupakuzi Vangipuram and J. Zhang, 450 nm Gallium Nitride Alternating Current Light-Emitting Diode, *IEEE Photonics J.*, 2020, **12**(6), 1–6.
54 K. Wang, Y. Liu, C. Wu, D. Li, S. Lv, Y. Zhang, X. Zhou and T. Guo, Electroluminescence from muLED without external charge injection, *Sci. Rep.*, 2020, **10**(1), 8059.
55 R. W. Hughes and M. Warner, LEDs driven by AC without transformers or rectifiers, *Sci. Rep.*, 2021, **11**(1), 963.
56 K. Wang, P. Chen, J. Chen, Y. Liu, C. Wu, J. Sun, X. Zhou, Y. Zhang and T. Guo, Alternating current electroluminescence from GaN-based nanorod light-emitting diodes, *Opt. Laser Technol.*, 2021, **140**, 107044.

57 C.-Y. Chang, C.-L. Yu, C.-A. Lin, H.-T. Lin, A. B. Lee, Z.-Z. Chen, L.-S. Lu, W.-H. Chang, H.-C. Kuo and M.-H. Shih, Hybrid Composites of Quantum Dots, Monolayer WSe2, and Ag Nanodisks for White Light-Emitting Diodes, *ACS Appl. Nano Mater.*, 2020, **3**(7), 6855–6862.

58 N. Taghipour, P. L. Hernandez Martinez, A. Ozden, M. Olutas, D. Dede, K. Gungor, O. Erdem, N. K. Perkgoz and H. V. Demir, Near-Unity Efficiency Energy Transfer from Colloidal Semiconductor Quantum Wells of CdSe/CdS Nanoplatelets to a Monolayer of MoS2, *ACS Nano*, 2018, **12**(8), 8547–8554.

59 O. Karni, E. Barre, S. C. Lau, R. Gillen, E. Y. Ma, B. Kim, K. Watanabe, T. Taniguchi, J. Maultzsch, K. Barmak, R. H. Page and T. F. Heinz, Infrared Interlayer Exciton Emission in MoS_2/WSe_2 Heterostructures, *Phys. Rev. Lett.*, 2019, **123**(24), 247402.

60 S. Zhang, C. G. Wang, M. Y. Li, D. Huang, L. J. Li, W. Ji and S. Wu, Defect Structure of Localized Excitons in a WSe_{2} Monolayer, *Phys. Rev. Lett.*, 2017, **119**(4), 046101.

61 M. Paur, A. J. Molina-Mendoza, R. Bratschitsch, K. Watanabe, T. Taniguchi and T. Mueller, Electroluminescence from multi-particle exciton complexes in transition metal dichalcogenide semiconductors, *Nat. Commun.*, 2019, **10**(1), 1709.

62 F. Ahmed, M. S. Choi, X. Liu and W. J. Yoo, Carrier transport at the metal-MoS2 interface, *Nanoscale*, 2015, **7**(20), 9222–9228.

63 J. R. Duran Retamal, D. Periyanagounder, J. J. Ke, M. L. Tsai and J. H. He, Charge carrier injection and transport engineering in two-dimensional transition metal dichalcogenides, *Chem. Sci.*, 2018, **9**(40), 7727–7745.

64 C. Herring and M. H. Nichols, Thermionic Emission., *Rev. Mod. Phys.*, 1949, **21**(2), 185–270.

65 W. Schottky, Emission of Electrons from an Incandescent Filament Under the Action of a Retarding Potential, *Ann. Phys.*, 1914, **44**, 1011–1032.

66 J. G. Simmons, Generalized Formula for the Electric Tunnel Effect between Similar Electrodes Separated by a Thin Insulating Film, *J. Appl. Phys.*, 1963, **34**(6), 1793–1803.

67 E. L. Wolf, *Principles of electron tunneling spectroscopy*, Oxford University Press, Oxford, U.K, 1985.

68 J.-R. Chen, P. M. Odenthal, A. G. Swartz, G. C. Floyd, H. Wen, K. Y. Luo and R. K. Kawakami, Control of Schottky Barriers in Single Layer MoS2 Transistors with Ferromagnetic Contacts, *Nano Lett.*, 2013, **13**(7), 3106–3110.

69 D. H. Jung, S.-i. Kim and T. Kim, Characteristics of electrical metal contact to monolayer WSe2, *Thin Solid Films*, 2021, **719**, 138508.

70 N. Kaushik, A. Nipane, F. Basheer, S. Dubey, S. Grover, M. M. Deshmukh and S. Lodha, Schottky barrier heights for Au and Pd contacts to MoS2, *Appl. Phys. Lett.*, 2014, **105**(11), 113505.

71 D. Hu, X. Xu, J. Miao, O. Gidron and H. Meng, A Stretchable Alternating Current Electroluminescent Fiber, *Materials*, 2018, **11**(2), 184.

72 P. D. Rack and P. H. Holloway, The structure, device physics, and material properties of thin film electroluminescent displays, *Mater. Sci. Eng., R*, 1998, **21**, 171–219.

73 L. Wang, L. Xiao, H. Gu and H. Sun, Advances in Alternating Current Electroluminescent Devices, *Adv. Opt. Mater.*, 2019, **7**, 1801154.

74 L.-C. Chen, C.-H. Hsu, X. Zhang and J.-R. Wu, Low-Cost ZnO:YAG-Based Metal-Insulator-Semiconductor White Light-Emitting Diodes with Various Insulators, *Int. J. Photoenergy*, 2014, 1–4.